Available online at www.sciencedirect.com

SciVerse ScienceDirect

Ceramics International 38 (2012) 1991–1998

CERAMICS INTERNATIONAL

www.elsevier.com/locate/ceramint

Interfacial characterization of YSZ-to-steel joints with Ag–Cu–Pd interlayers for solid oxide fuel cell applications

Kun-Lin Lin [a,*], Mrityunjay Singh [b], Rajiv Asthana [c]

[a] National Nano Device Laboratories, Hsinchu 300, Taiwan
[b] Ohio Aerospace Institute, Cleveland, OH 44142, USA
[c] Engineering and Technology Dept., University of Wisconsin-Stout, Menomonie, WI 54751, USA

Received 4 October 2011; accepted 12 October 2011
Available online 18 October 2011

Abstract

Yttria-stabilized zirconia (YSZ)/stainless steel joints made using two commercial silver-based interlayers containing palladium (58Ag–32Cu–10Pd and 65Ag–20Cu–15Pd), were systematically analyzed for the microstructures of the interlayer matrices, interlayer–steel interface, and interlayer–YSZ interface using scanning electron microscopy (SEM) and transmission electron microscopy coupled with energy dispersive spectroscopy (TEM/EDS). In the interlayer matrix, a face-centered cubic (FCC) Cu-rich phase formed in the vicinity of the YSZ and dissolved a significant amount of Zr from the ZrO_2 and minor amounts of Fe and Cr from the steel. The Cu-rich phase in the interlayer matrix in the vicinity of the steel substrate was the ordered phase Cu_3Pd with antiphase boundaries (APBs) and the $L1_2$ crystal structure. Silver particles precipitated within the Cu_3Pd phase in 58Ag–32Cu–10Pd; a Fe(Cr) needle-like phase, instead of Ag particles, precipitated within the Cu_3Pd phase in 65Ag–20Cu–15Pd. Although no reaction products at the interlayer–steel interface were found, dislocations appeared within the Ag- and Cu-rich phases. At the interlayer–YSZ interface, two reaction products, SiO_2 (impurity in YSZ) and Ti_3O_5 (from the reaction of YSZ with Ti impurities in the steel) were observed. Diffusion and chemical reactions led to the compositional changes and interface reconstruction, thereby yielding metallurgically sound YSZ/steel joints.

Keywords: B. Microstructures; B. Interfaces; Ag–Cu–Pd interlayer; Transmission electron microscopy; SOFC; Joint

1. Introduction

The joining of ceramics and metals in solid oxide fuel cells (SOFCs) is a critical and important step during their manufacture. The ceramic/metal joints in SOFCs require high strength, good wetting, and resistance to grain coarsening and thermomechanical degradation [1,2]. Diffusion bonding, friction welding, transient liquid-phase (TLP) bonding, and brazing are commonly used for ceramic/ceramic and ceramic/metal joining [3]. Active metal brazing is a cost-effective approach toward creating structurally sound ceramic–ceramic and ceramic–metal joints. Active braze fillers must enable wetting, spreading, and bonding to occur without metallurgically degrading the joint. Zirconia is most commonly used in the electrolyte materials of SOFCs; it is also joined with metals for specific applications in SOFCs. Scanning electron microscopy (SEM), energy dispersive spectroscopy (EDS), and X-ray diffraction (XRD) have been employed to examine the microstructures and reaction products at the interfaces and in the interlayers of zirconia–metal or zirconia–zirconia joints prepared using active brazes, such as Ag-based [4–6], Cu-based [4,7], Au-based [8], and Pd-based [9,10] metal fillers. Nevertheless, it is not possible to reveal the finer details of the joint microstructures at greater resolution when using these techniques.

In this study, transmission electron microscopy equipped with an energy dispersive spectrometer (TEM/EDS) was used to analyze yttria-stabilized zirconia (YSZ)-to-stainless steel joints. Two electrically conductive Ag-based commercial interlayers (58Ag–32Cu–10Pd and 65Ag–20Cu–15Pd) containing palladium as an alloying element with electrical conductivities of 18.9×10^6 and $13.0 \times 10^6\ \Omega^{-1}\ m^{-1}$, respectively, were used to join YSZ and stainless steel for possible applications in SOFC interconnects. Palladium offers high use-temperatures and good resistance against oxidation. Although

---

* Corresponding author.
E-mail address: kllin@ndl.narl.org.tw (K.-L. Lin).

0272-8842/$36.00 © 2011 Elsevier Ltd and Techna Group S.r.l. All rights reserved.
doi:10.1016/j.ceramint.2011.10.033

Ag, Cu, and Pd have weak affinity for ZrO_2 and form large contact angles (148°, 147°, and 98° at 1273, 1423, and 1833 K [11], respectively), they have been successfully used to join YSZ [9,10].

Selected area diffraction patterns (SADPs) in TEM and EDS were used to identify the crystal structures of the new phases or precipitates and to propose their orientation relationships with the interlayer matrices and the interlayer–steel and interlayer–YSZ interfaces.

2. Experimental procedure

A corrosion-resistant ferritic stainless steel (Allegheny Ludlum) and YSZ substrates containing 3 mol% yttria were used in the joining experiments. The steel nominally contained 17–19% Cr and minor alloying constituents (<0.1% Mn, P, Si, Ni, and Ti). The YSZ substrates (~1.63 mm) were prepared by tape-casting and stacking four of the tape-cast layers, followed by sintering. Two Ag-based metallic interlayers containing Cu and Pd as alloying elements, 58Ag–32Cu–10Pd and 65Ag–20Cu–15Pd (numbers represent compositions in wt%; Morgan Advanced Ceramics, Hayward, CA), were obtained in foil form (thickness: 0.1–0.12 mm) and used to study the effect of the Pd content on the joint microstructure and composition.

The brazing procedure consisted of placing a metallic interlayer between YSZ and stainless-steel coupons (each 1.27 cm × 1.27 cm) under a normal load of approximately 0.3 N. All materials were pre-cleaned in acetone (ultrasonication for 10 min) to remove surface contaminants. The sample assembly was heated under a vacuum ($\sim10^{-6}$ Torr) to the brazing temperature (approximately 20 °C above the braze liquidus), held isothermally at the brazing temperature for 5 min, and then cooled to room temperature at a controlled rate. The cross-sectional TEM specimens of YSZ/interlayer/steel joints were cut, ground, polished and then ion milled by standard procedures. The microstructures were characterized using a JSM-6330F scanning electron microscope (JEOL, Tokyo, Japan) and a JEM 2010Fx transmission electron microscope (JEOL, Tokyo, Japan) equipped with an ISIS300 energy dispersive spectrometer (Oxford Instrument, London, UK). Quantitative composition analyses were performed based on the principles of the Cliff–Lorimer [12] standardless method.

3. Results and discussion

3.1. SEM analysis

Fig. 1(a) displays a backscattered electron image (BEI) of the steel/58Ag–32Cu–10Pd/YSZ joint. Two main phases, dark and white areas, within the 58Ag–32Cu–10Pd interlayer were observed. In the Ag–Cu system [13], after cooling, the dark area was a Cu-rich phase and the light area was a Ag-rich phase. Small spherical particles (marked with arrows in Fig. 1) formed in both the Cu- and Ag-rich matrices. In the Cu-rich areas, white spherical particles formed near the steel; their abundance gradually decreased upon approaching the YSZ. In contrast, dark spherical particles formed in the Ag-rich areas. In the steel/65Ag–20Cu–15Pd/YSZ joint [Fig. 1(b)], needle-like precipitates formed in the Cu-rich areas, in contrast to the white spherical particles that had formed in the steel/58Ag–32Cu–10Pd/YSZ joint [Fig. 1(a)]; the dark spherical particles formed in the Ag-rich matrices of both joints. The abundance of the needle-like precipitates in the Cu-rich areas gradually decreased upon progressing away from the steel toward the YSZ; these precipitates formed due to elemental dissolution of the steel constituents (e.g., Fe and Cr) in the interlayer. Different variants of the needle-like precipitates formed within the matrix, as indicated by the arrows in an enlarged image in the inset to Fig. 1(b). At the steel–interlayer and interlayer–YSZ interfaces, no obvious reaction layer formation occurred, as evidenced by the SEM images in Fig. 1(a) and (b).

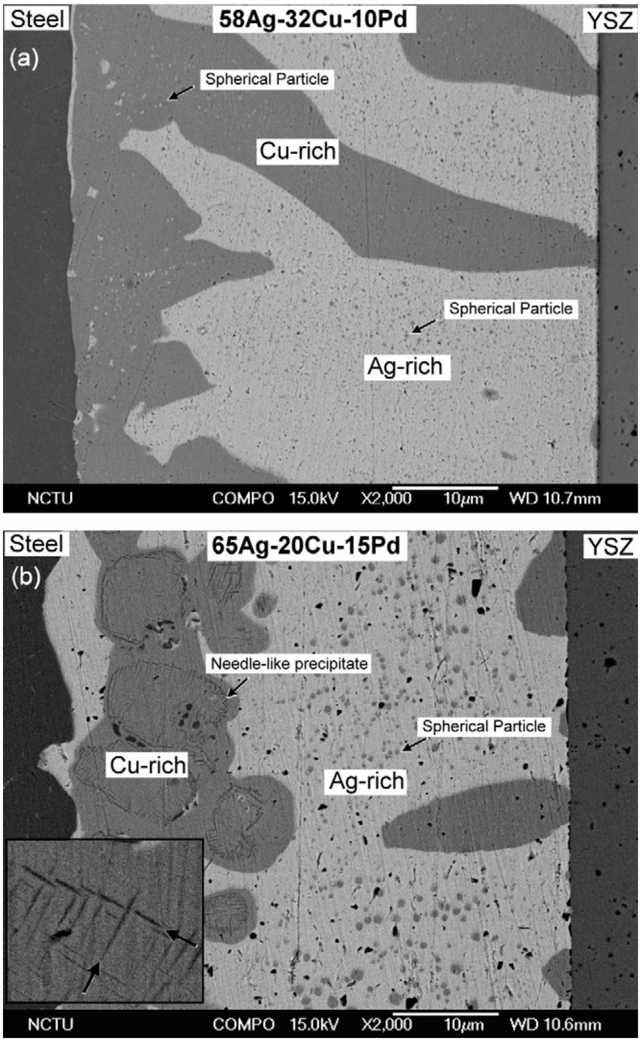

Fig. 1. Scanning electron micrographs (backscattered electron image, BEI) of the (a) steel/58Ag–32Cu–10Pd/YSZ and (b) steel/65Ag–20Cu–15Pd/YSZ joints.

3.2. TEM analysis

3.2.1. Ag-rich matrix in interlayer

Fig. 2(a) presents a BFI (bright-field image) of a Cu particle within the Ag-rich matrix in the steel/58Ag–32Cu–10Pd/YSZ

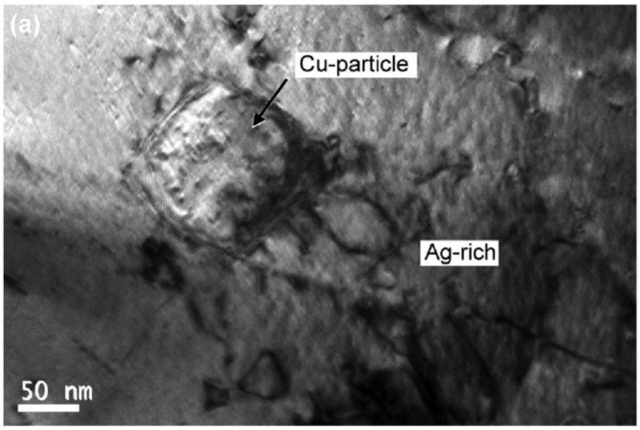

(b)

Atomic %	Ag	Cu	Fe	Cr	Pd	Zr
Cu-particle	3.8	79.8	2.2	1.5	9.8	2.9
Ag-rich	72.6	14.7	6.0	2.1	x	4.6

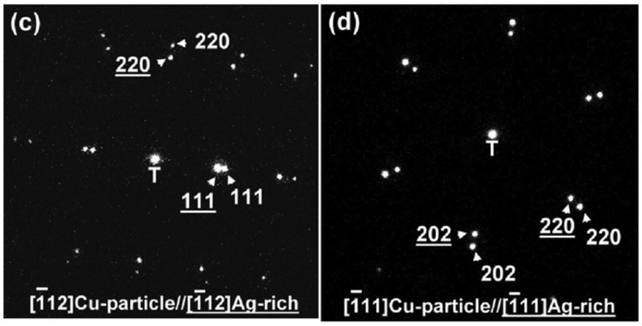

Fig. 2. (a) Transmission electron micrograph (BFI) of the Cu particle within the Ag-rich phase in the steel/58Ag–32Cu–10Pd/YSZ joint. (b) Chemical compositions of the Cu particle and the Ag-rich phase. (c, d) SADPs of the Cu particle and Ag-rich phase with zone axes of $[\bar{1}\,1\,2]_{\text{Cu-particle}}//[\bar{1}\,1\,2]_{\text{Ag-rich}}$ and $[\bar{1}\,1\,1]_{\text{Cu-particle}}//[\bar{1}\,1\,1]_{\text{Ag-rich}}$, respectively.

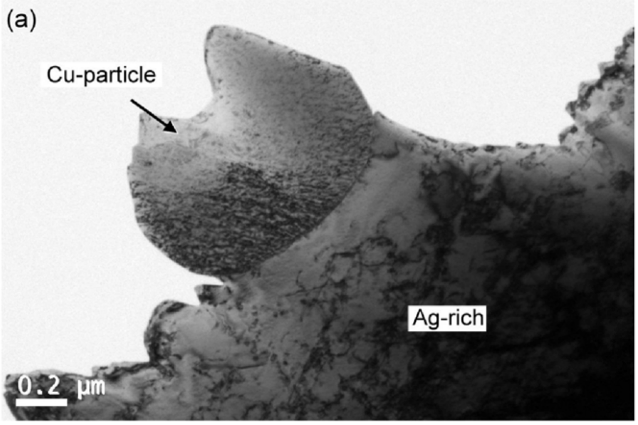

(b)

Atomic %	Ag	Cu	Fe	Cr	Pd	Zr
Cu-particle	2.8	72.5	3.4	1.3	19.0	1.0
Ag-rich	81.9	7.9	4.1	1.5	2.5	2.1

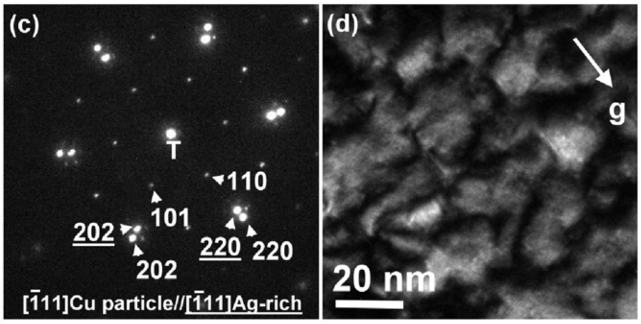

Fig. 3. (a) Transmission electron micrograph (BFI) of the Cu particle within the Ag-rich phase in the steel/65Ag–20Cu–15Pd/YSZ joint. (b) Chemical compositions of the Cu particle and the Ag-rich phase. (c) SADPs of the Cu particle and Ag-rich phase with zone axes of $[\bar{1}\,1\,1]_{\text{Cu-particle}}//[\bar{1}\,1\,1]_{\text{Ag-rich}}$. (d) Dark-field image in the [1 1 0] reflection, revealing the presence of an APB in the Cu particle.

joint, corresponding to the dark spherical particles in the Ag-rich regions of Fig. 1(a). From the EDS analysis in Fig. 2(b), the spherical particle is Cu-rich and the matrix is Ag-rich. Fig. 2(c) and (d) display the superimposed SADPs of the Cu-rich particle and the Ag-rich matrix with zone axes of $[\bar{1}\,1\,2]_{\text{Cu-particle}}//[\bar{1}\,1\,2]_{\text{Ag-rich}}$ and $[\bar{1}\,1\,1]_{\text{Cu-particle}}//[\bar{1}\,1\,1]_{\text{Ag-rich}}$, respectively. The crystal structures of the Cu particle and Ag-rich matrix are face-centered cubic (FCC) and their orientation relationship is cube-on-cube. The lattice parameters of pure Cu and Ag are 0.362 and 0.408 nm, respectively; for the Cu particle and Ag-rich matrix in our joints, the values were calculated as 0.374 and 0.418 nm, respectively. Obviously, the lattice parameters of the Cu-rich particle and Ag-rich matrix increased as a result of the other dissolved elements (e.g., Fe, Cr, Pd, Zr) from the steel or the YSZ. The cube-on-cube orientation appeared at the interface between the Cu matrix and the Ag in the Cu–71.8 wt% Ag alloy system. The lattice parameters also indicate that the lattice misfit between the Cu and Ag phases will result in dislocations at the interface between the two phases [13].

Fig. 3(a) displays a BFI of a Cu particle within the Ag-rich matrix in the steel/65Ag–20Cu–15Pd/YSZ joint, corresponding to the dark spherical particles in the Ag-rich matrix in Fig. 1(b). The EDS analysis in Fig. 3(b) reveals that the particle was Cu-rich and the matrix was Ag-rich. Notably, a large amount of Pd (19.0 at.%) had dissolved in the Cu particle. Several researchers have mentioned that Cu–Pd FCC solid solution undergoes ordering reactions in the range of 10–30 at.% Pd [14–16]. During cooling, the ordering phase is Cu_3Pd with an antiphase boundary (APB) and the crystal structure is $L1_2$. Fig. 3(c) presents the SADP of a Cu particle and the Ag-matrix with $[\bar{1}\,1\,1]_{\text{Cu-particle}}//[\bar{1}\,1\,1]_{\text{Ag-rich}}$, indicating that the superlattice spots (1 1 0) and (1 0 1) appear in the Cu particle's diffraction pattern compared with Fig. 2(d); these spots are a forbidden reflection for FCC Cu. From the SADP and EDS data, the Cu particle is Cu_3Pd with an $L1_2$ crystal structure and has a cube-on-cube orientation relationship with the Ag-rich matrix. The lattice parameters of the Cu-rich (Cu_3Pd) particle and the Ag-rich matrix were calculated to be 0.392 and 0.435 nm, respectively. The lattice parameter of the Cu-rich (Cu_3Pd) particle is 8.4% greater than that of pure Cu, presumably because of the large degree of Pd dissolution (19.0 at.%). The Cu_3Pd particle featured an APB, as evidenced by a dark-field image along with the [1 1 0] reflection in Fig. 3(d).

To summarize, fine Cu particles having a FCC crystal structure precipitated in the Ag-rich matrix in the 58Ag–32Cu–10Pd interlayer after cooling; the relationship between the two phases was cube-on-cube. Upon increasing the Pd content to 15 wt% in the interlayer (65Ag–20Cu–15Pd), ordered Cu_3Pd particles, instead of Cu-rich particles, precipitated in the Ag-rich matrix; again, the orientation relationship between the Cu_3Pd particles and the Ag-rich matrix was also cube-on-cube.

3.2.2. Cu-rich matrix in interlayer

Fig. 4(a) displays a BFI of an Ag particle in the Cu-rich matrix within the steel/58Ag–32Cu–10Pd/YSZ joint, corresponding to the white particles in the Cu-rich matrix in Fig. 1(a). EDS analysis [Fig. 4(b)] revealed a large amount of Pd (18 at.%) in the Cu-rich matrix. Fig. 4(c) presents the SADP of a Ag particle and the Cu-matrix with $[0\ 1\ 1]_{\text{Ag-particle}}//[0\ 1\ 1]_{\text{Cu-rich}}$; the superlattice spots (1 0 0) and $(0\ \bar{1}\ 1)$ appear in the diffraction pattern of the Cu-rich matrix. The Cu-rich matrix near the steel had the Cu_3Pd phase and the orientation relationship between the Ag particles and the Cu_3Pd phase was cube-on-cube, similar to that of the Cu or Cu_3Pd particles in the Ag-rich matrix [Figs. 2(c, d), and 3(c)]. The lattice parameters of the Ag particles and the Cu_3Pd phase were 0.430 and 0.390 nm, respectively. An APB appeared in the Cu_3Pd phase, as evidenced in Fig. 4(d) by a dark-field image along the $[0\ \bar{1}\ 1]$ reflection of Fig. 4(c).

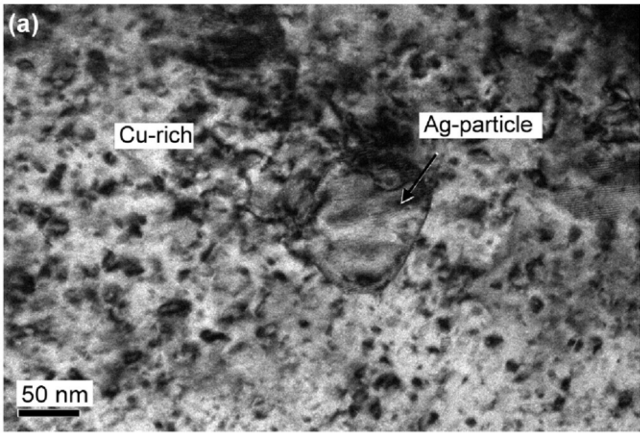

(b)

Atomic %	Ag	Cu	Fe	Cr	Pd	Zr
Ag-particle	72.8	12.5	7.3	2.5	1.3	3.7
Cu-rich	1.8	70.9	6.3	1.0	18.0	2.0

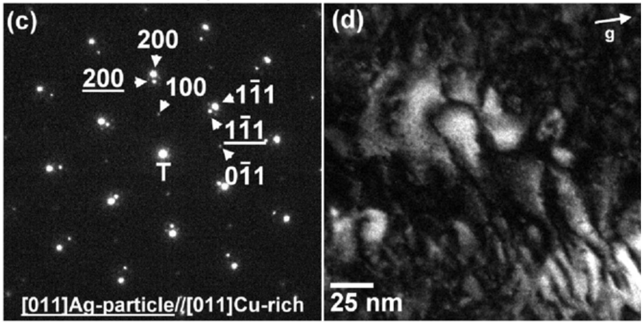

Fig. 4. (a) Transmission electron micrograph (BFI) of an Ag particle within the Cu-rich phase in the steel/58Ag–32Cu–10Pd/YSZ joint. (b) Chemical compositions of the Ag particle and the Cu-rich phase. (c) SADPs of the Ag particle and the Cu-rich phase with zone axes of $[0\ 1\ 1]_{\text{Ag-particle}}//[0\ 1\ 1]_{\text{Cu-rich}}$. (d) Dark-field image in the $[0\ \bar{1}\ 1]$ reflection, revealing the presence of an APB in the Cu-rich phase.

Fig. 5(a) presents the BFI of the Cu-rich matrix within the 65Ag–20Cu–15Pd interlayer; it reveals needle-like Fe(Cr) phase precipitates (with three variants marked by arrows in Fig. 5a) corresponding to the Cu-rich regions in the SEM image of Fig. 1(b). Large amounts of Fe and Cr had dissolved in the Cu-rich matrix, resulting in a supersaturated Cu-rich matrix from which the Fe(Cr) phase precipitated upon cooling. Fig. 5(b) reveals the composition of the Fe(Cr) needle-like phase and the Cu-rich matrix. Fig. 5(c)–(e) present the SADPs of the Fe(Cr) phase and the Cu-rich (Cu_3Pd) phase, along with zone axes of $[1\,0\,\bar{1}]_{\text{Fe(cr)}}//[0\,0\,1]_{\text{Cu-rich}}$, $[1\,\bar{1}\,0]_{\text{Fe(cr)}}//[0\,1\,0]_{\text{Cu-rich}}$, and $[1\ 1\ 0]_{\text{Fe(cr)}}//[1\ 0\ 0]_{\text{Cu-rich}}$, respectively. The Cu-rich phase was Cu_3Pd, as evidenced by the large degree of Pd dissolution (35 at.%) and the appearance of superlattice spots in the SADPs of the Cu-rich matrices. From the SADP and EDS data, the Fe(Cr) phase was body-centered cubic (BCC) and the Cu-rich phase was Cu_3Pd with an $L1_2$ crystal structure. In addition, the orientation of the Fe(Cr) and Cu-rich phases had a Bain relationship. Fig. 6(a)–(c) display schematic representations of the Fe(Cr) and Cu-rich

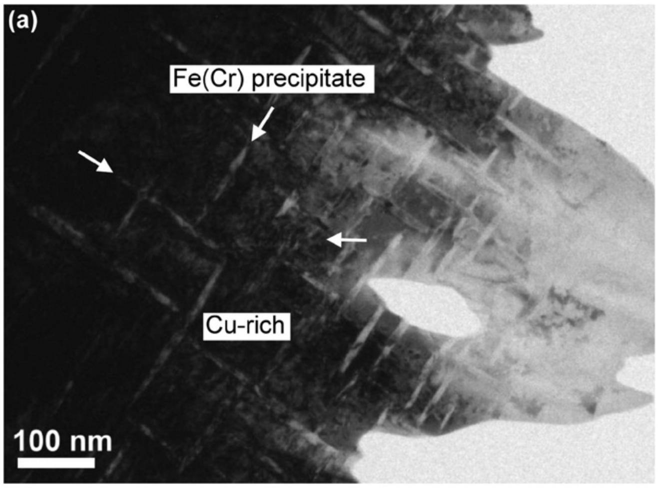

(b)

Atomic %	Ag	Cu	Fe	Cr	Pd	Zr
Fe(Cr) precipitate	0.3	3.1	75.7	16.3	4.4	0.2
Cu-rich	3.5	31.2	24.8	4.4	35.0	1.1

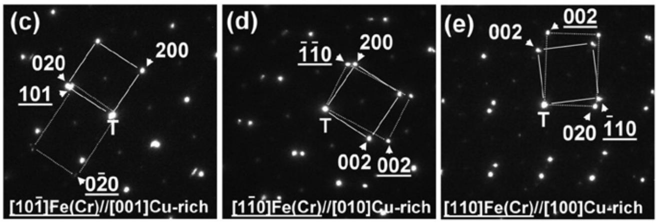

Fig. 5. (a) Transmission electron micrograph (BFI) of the Fe(Cr) precipitate in the Cu-rich phase with three variants, indicated by the arrows, in the steel/65Ag–20Cu–15Pd/YSZ joint. (b) Chemical compositions of the Fe(Cr) precipitate and the Cu-rich phase. (c–e) SADPs of the Fe(Cr) precipitate and the Cu-rich phase with zone axes of (c) $[1\,0\,\bar{1}]_{\text{Fe(cr)}}//[0\,0\,1]_{\text{Cu-rich}}$, (d) $[1\,\bar{1}\,0]_{\text{Fe(cr)}}//[0\,1\,0]_{\text{Cu-rich}}$, and (e) $[1\ 1\ 0]_{\text{Fe(cr)}}//[1\ 0\ 0]_{\text{Cu-rich}}$.

(Cu_3Pd) phases with three variants: $[1\,0\,\bar{1}]_{\mathrm{Fe(cr)}}//[0\,0\,1]_{\mathrm{Cu\text{-}rich}}$, $[1\,\bar{1}\,0]_{\mathrm{Fe(cr)}}//[0\,1\,0]_{\mathrm{Cu-rich}}$, and $[1\ 1\ 0]_{\mathrm{Fe(cr)}}//[1\ 0\ 0]_{\mathrm{Cu\text{-}rich}}$ according to the SADPs of Fig. 5(c)–(e). The Bain relationship of the FCC to BCC transformation with three types of Bain variants has been proposed in the corresponding iron system [17,18]. They indicate that the FCC to BCC Bain transformation is a martensitic phase transformation that accompanies crystal structure distortion or a rigid body rotation. From the SADPs in Fig. 5(d) and (e), the angle between the (0 0 2) planes of the Fe(Cr) and Cu-rich phases was rotated approximately 9.7°, suggesting that the Fe(Cr) crystal structure formed in the Cu_3Pd phase was accompanied by either rotation or distortion.

The Cu-rich phases in the 58Ag–32Cu–10Pd and 65Ag–20Cu–15Pd interlayers near the steel had different microstructures. According to the Cu–Ag phase diagram, Ag particles precipitated with a cube-on-cube relationship in the Cu-rich regions of the 58Ag–32Cu–10Pd interlayer because of a decrease in the solubility of Ag in Cu during cooling [19]. Upon increasing the Pd content to 15 wt% in 65Ag–20Cu–15Pd, however, large amounts of Fe and Cr dissolved in the Cu-rich matrix, resulting in the precipitation of the Fe(Cr) phase in the Cu-rich matrix with three variants and the orientation relationship similar to that of the Bain transformation. The EDS data in Figs. 4(b) and 5(b) revealed that approximately 10 wt% of Pd effectively inhibited the diffusion of Fe (6.3 at.%) and Cr (1.0 at.%) into the Cu-rich matrix of 58Ag–32Cu–10Pd, thereby suppressing the formation of the needle-like Fe(Cr) phase. In contrast, the higher (15 wt%) Pd content in 65Ag–20Cu–15Pd aided the diffusion and redistribution of Fe (24.8 at.%) and Cr (4.4 at.%) in the Cu-rich matrix of the interlayer, leading to the formation of needle-like Fe(Cr) phases within the Cu-rich matrix. Here, the Cu-rich phase dissolved a large amount of Pd (18–35 at.%) and underwent transformation into the ordered $L1_2$-type Cu_3Pd phase with APBs upon cooling.

3.2.3. Interlayer/steel interface

Fig. 7(a) presents a BFI of the interlayer–steel interface in a steel/58Ag–32Cu–10Pd/YSZ joint; it reveals good metallurgical continuity in the interfacial region and the absence of any reaction product at the interface. The chemical compositions of the steel and the Ag- and Cu-rich phases [Fig. 7(b)] indicate the dissolution of Fe and Cr into both the Ag- and Cu-rich phases. Fig. 7(c)–(e) display the SADPs of the steel (α-Fe, BCC), the Ag-rich phase, and the Cu-rich phase with zone axes of [0 0 1], [0 1 1], and [0 1 1], respectively. The lattice parameters of α-Fe, the Ag-rich phase, and the Cu-rich phase were calculated to be 0.292, 0.410, and 0.378 nm, respectively. Comparisons with the lattice parameters of pure α-Fe (0.287 nm), pure Ag (0.408 nm), and pure Cu (0.362 nm) reveal degrees of lattice expansion of α-Fe, the Ag-rich phase, and the Cu-rich phase of 1.7, 0.5, and 4.4%, respectively. The Cu-rich phase dissolved a large amount of Pd (18 at.%) and formed the Cu_3Pd phase upon cooling. The Cu_3Pd phase with the APB structure is displayed in a dark-field image with $[0\,\bar{1}\,1]$ reflection in Fig. 7(f).

Fig. 8(a) presents a BFI of the transmission electron micrograph of the interlayer–steel interface in the steel/65Ag–20Cu–15Pd/YSZ joint. A microstructurally sound joint devoid of interfacial voids and microcracks had formed. Nevertheless, dislocations appear in the Ag- and Cu-rich phases, due to a mismatch in the coefficient of thermal expansion (CTE) between the interlayer and the steel. The chemical compositions of the steel and the Ag- and Cu-rich phases [Fig. 8(b)] indicate that 19.8 at.% of Pd had dissolved in the Cu-rich phase, thereby forming a ordered Cu_3Pd phase with an $L1_2$ crystal structure. Fig. 8(c)–(e) present SADPs of the steel (α-Fe) with a zone axis of [1 1 1], the Ag-rich phase with a zone axis of [0 1 1], and the Cu-rich phase with a zone axis of [0 0 1], respectively. The lattice parameters of the α-Fe, the Ag-rich phase, and the Cu-rich phase were 0.300, 0.411, and 0.391 nm, respectively; their degrees of lattice expansion were 4.5, 0.7, and 8.0%, respectively. Therefore, the degrees of lattice expansion of the α-Fe, the Ag-rich phase, and the Cu-rich phase in 65Ag–20Cu–15Pd were larger than those in 58Ag–32Cu–10Pd. In addition, the Cu-rich phase was Cu_3Pd and the APBs were also evident in the dark-field image in Fig. 8(f).

3.2.4. Interlayer/YSZ interface

Fig. 9(a) provides a BFI of the interlayer–YSZ interface in a steel/58Ag–32Cu–10Pd/YSZ joint; it reveals dislocations in the Cu-rich phase and reaction products at the interlayer–YSZ interface. Fig. 9(b) displays the compositions of the Cu-rich

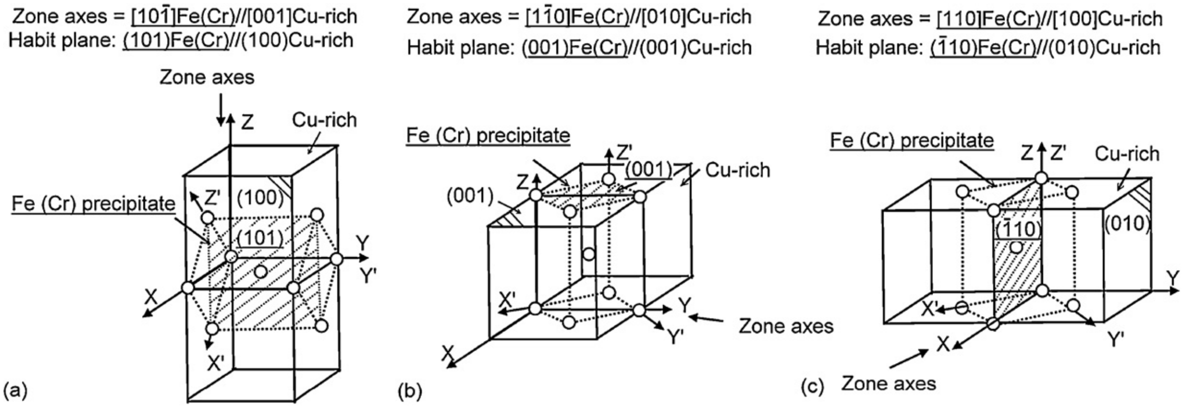

Fig. 6. Schematic representations of the Fe(Cr) precipitate and the Cu-rich phase: (a) $Z = [1\,0\,\bar{1}]_{\mathrm{Fe(cr)}}//[0\,0\,1]_{\mathrm{Cu-rich}}$; (b) $Z = [1\,\bar{1}\,0]_{\mathrm{Fe(cr)}}//[0\,1\,0]_{\mathrm{Cu-rich}}$; (c) $Z = [1\ 1\ 0]_{\mathrm{Fe(cr)}}//[1\ 0\ 0]_{\mathrm{Cu\text{-}rich}}$.

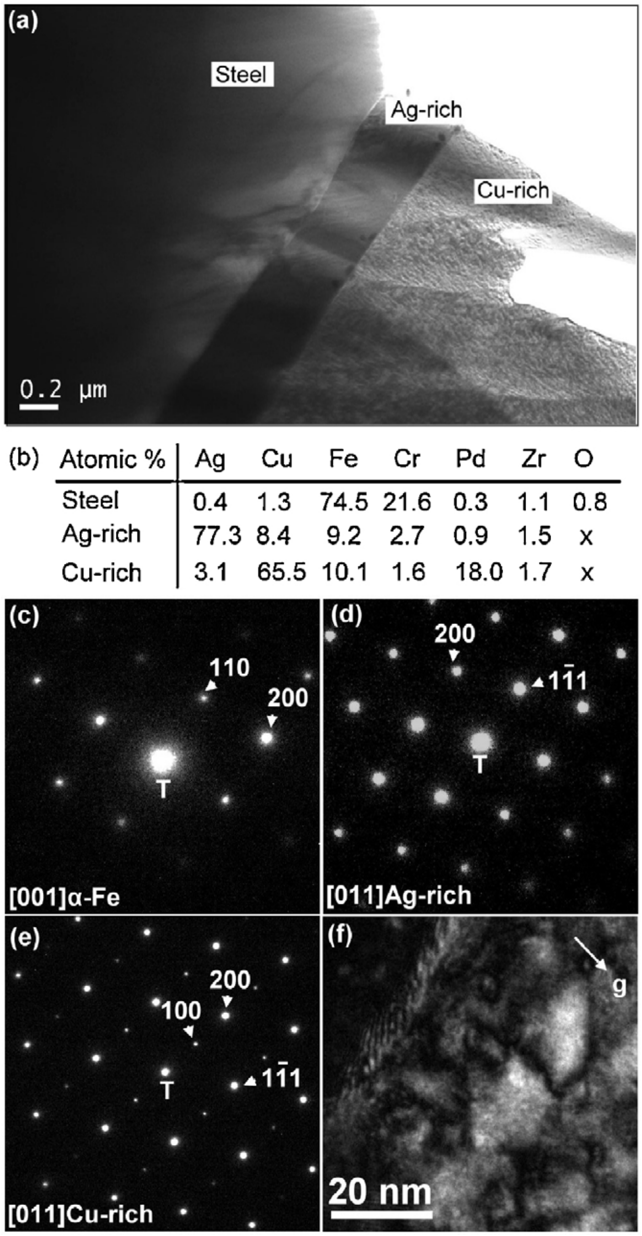

(b)

Atomic %	Ag	Cu	Fe	Cr	Pd	Zr	O
Steel	0.4	1.3	74.5	21.6	0.3	1.1	0.8
Ag-rich	77.3	8.4	9.2	2.7	0.9	1.5	x
Cu-rich	3.1	65.5	10.1	1.6	18.0	1.7	x

Fig. 7. (a) Transmission electron micrograph (BFI) of the interlayer–steel interface in the steel/58Ag–32Cu–10Pd/YSZ joint. (b) Chemical compositions of the steel and the Ag- and Cu-rich phases. (c–e) SADPs of (c) the steel (α-Fe; zone axis: [0 0 1]), (d) the Ag-rich phase (zone axis: [0 1 1]), and (e) the Cu-rich phase (zone axis: [0 1 1]). (f) Dark-field image in the $[0\,\bar{1}\,1]$ reflection, revealing the presence of an APB in the Cu-rich phase.

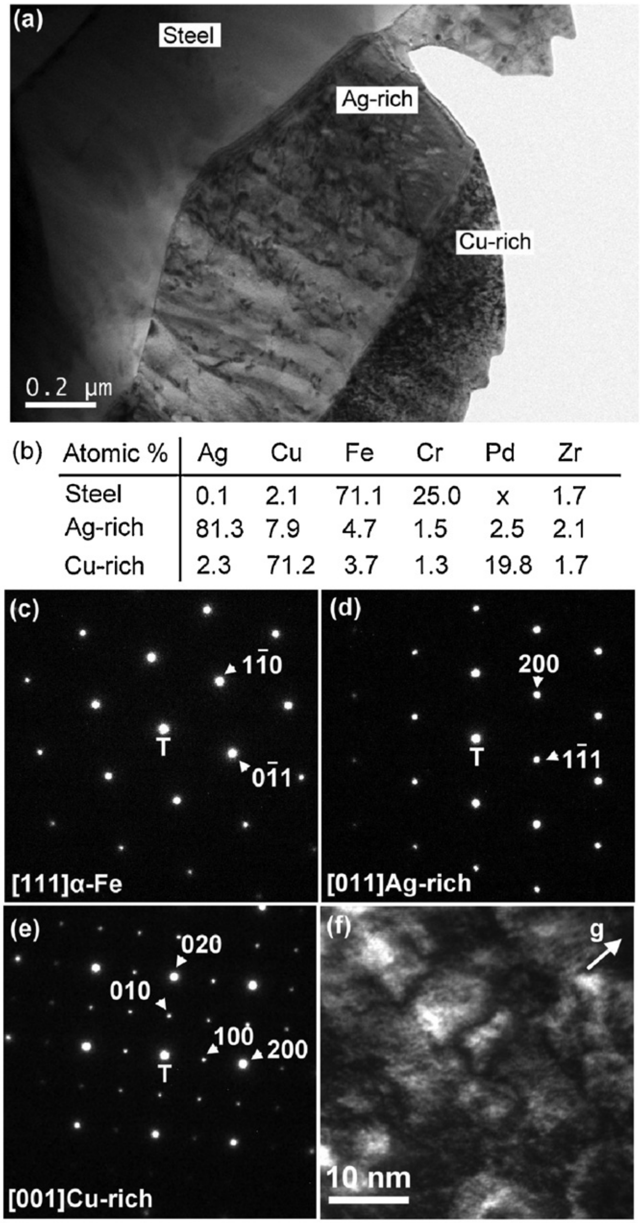

(b)

Atomic %	Ag	Cu	Fe	Cr	Pd	Zr
Steel	0.1	2.1	71.1	25.0	x	1.7
Ag-rich	81.3	7.9	4.7	1.5	2.5	2.1
Cu-rich	2.3	71.2	3.7	1.3	19.8	1.7

Fig. 8. (a) Transmission electron micrograph (BFI) of the interlayer–steel interface in the steel/65Ag–20Cu–15Pd/YSZ joint. (b) Chemical compositions of the steel and the Ag- and Cu-rich phases. (c–e) SADPs of (c) the steel (α-Fe; zone axis: [1 1 1]), (d) the Ag-rich phase (zone axis: [0 1 1]), and (e) the Cu-rich phase (zone axis: [0 0 1]). (f) Dark-field image in the [1 1 0] reflection, revealing the presence of an APB in the Cu-rich phase.

phase, the reaction products (Ti_3O_5 and SiO_2), and the YSZ, as determined through EDS analysis. In the Cu-rich phase, a large amount of Zr had dissolved from YSZ, but the Pd content was merely 0.2 at.%. From the SADP of the Cu-rich phase in Fig. 9(c) and the EDS data, very little Pd and no superlattice spots appeared in the diffraction pattern; therefore, the Cu-rich phase was FCC Cu and not Cu_3Pd. Interestingly, the Cu-rich phase near the steel was Cu_3Pd (18 at.%) with an $L1_2$ crystal structure [Fig. 7(b) and (e)], but the Cu-rich phase near YSZ was FCC Cu. Fig. 9(d) presents an SADP of the YSZ with the $[\bar{1}\,1\,1]$ zone axis of t-ZrO_2. Notably, however, {1 1 2}-type reflections appeared in the SADPs of t-ZrO_2 because the large concentration of oxygen vacancies altered the structure factor of t-ZrO_2. Meanwhile, the zirconia became blackened oxygen-deficient zirconia (ZrO_{2-x}) [5,20]. Fig. 9(e) provides a digital diffractogram obtained from a high-resolution image of amorphous SiO_2. Silica is the most common impurity present in YSZ, along with alumina and alkali metal oxides [21]. Thus, it was possible that amorphous SiO_2 gathered at the interface

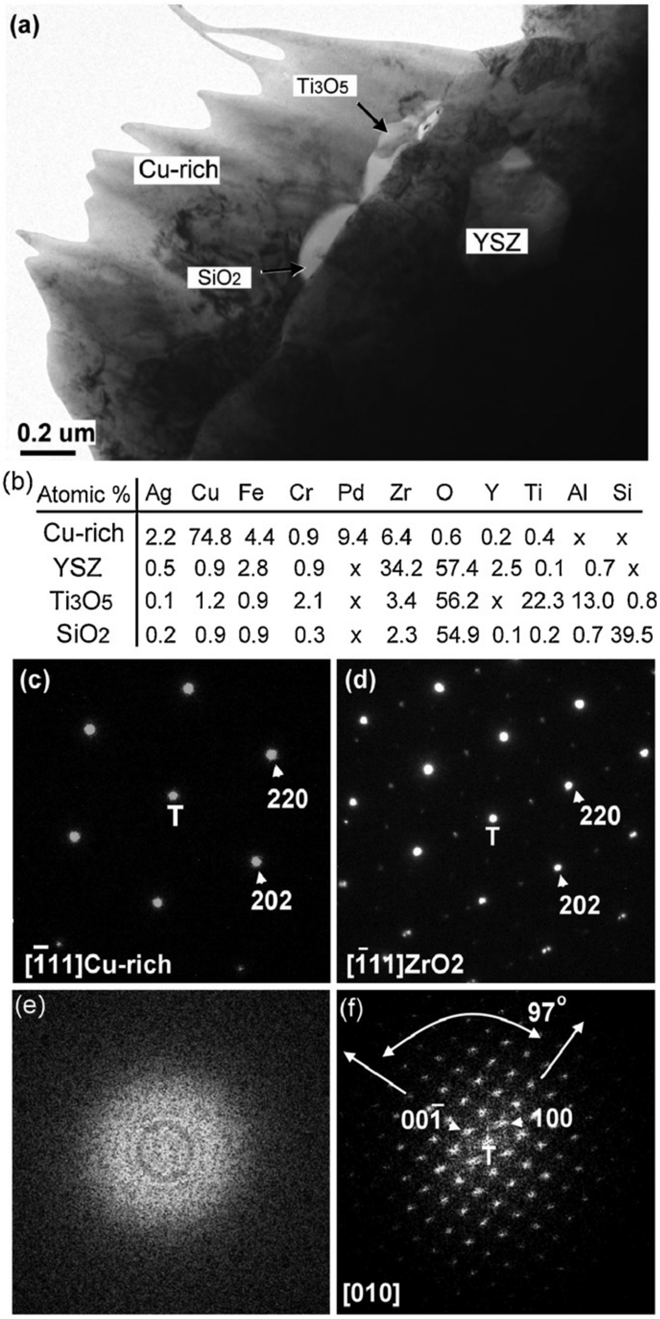

Atomic %	Ag	Cu	Fe	Cr	Pd	Zr	O	Y	Ti	Al	Si
Cu-rich	2.2	74.8	4.4	0.9	9.4	6.4	0.6	0.2	0.4	x	x
YSZ	0.5	0.9	2.8	0.9	x	34.2	57.4	2.5	0.1	0.7	x
Ti3O5	0.1	1.2	0.9	2.1	x	3.4	56.2	x	22.3	13.0	0.8
SiO2	0.2	0.9	0.9	0.3	x	2.3	54.9	0.1	0.2	0.7	39.5

Fig. 9. (a) Transmission electron micrograph (BFI) of the interlayer–YSZ interface in the steel/58Ag–32Cu–10Pd/YSZ joint. (b) Chemical compositions of the Cu-rich phase, the YSZ, Ti_3O_5, and SiO_2. (c, d) SADPs of (c) the Cu-rich phase (zone axis: $[\bar{1}\,1\,1]$) and (d) the YSZ (zone axis: $[\bar{1}\,1\,1]$). (e, f) Digital diffractograms obtained from high-resolution images of (e) amorphous SiO_2 and (f) Ti_3O_5 having a zone axis of [0 1 0].

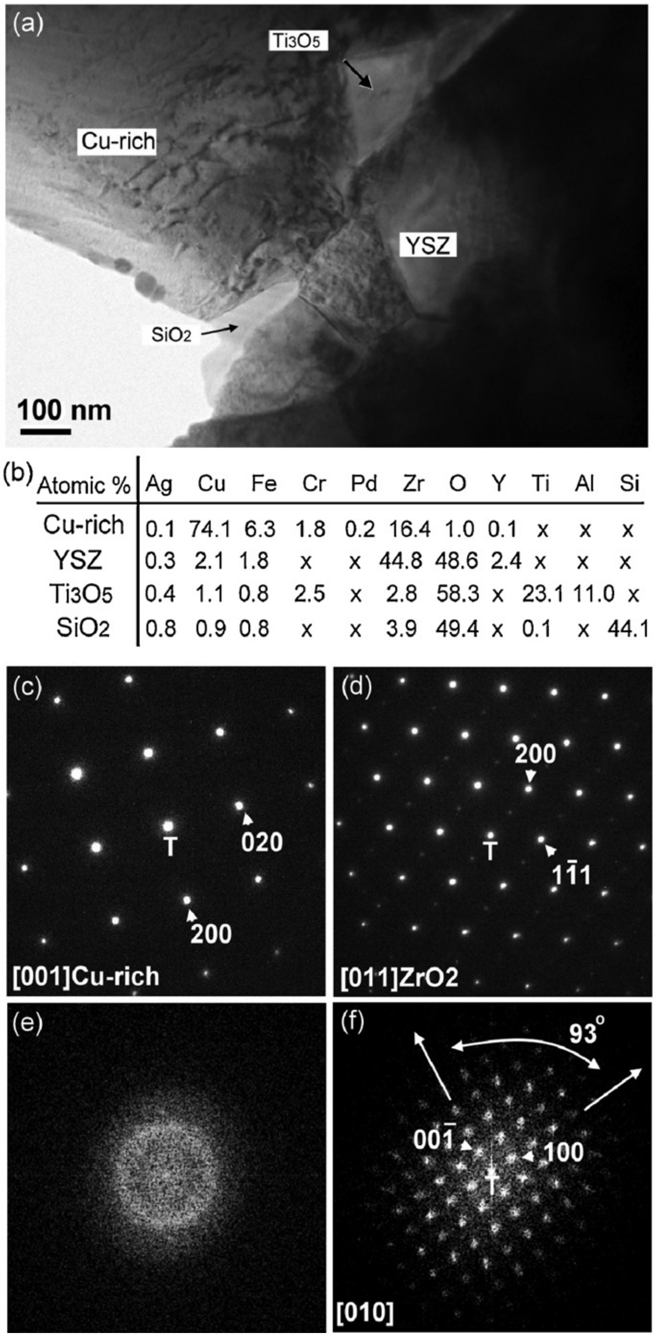

Atomic %	Ag	Cu	Fe	Cr	Pd	Zr	O	Y	Ti	Al	Si
Cu-rich	0.1	74.1	6.3	1.8	0.2	16.4	1.0	0.1	x	x	x
YSZ	0.3	2.1	1.8	x	x	44.8	48.6	2.4	x	x	x
Ti3O5	0.4	1.1	0.8	2.5	x	2.8	58.3	x	23.1	11.0	x
SiO2	0.8	0.9	0.8	x	x	3.9	49.4	x	0.1	x	44.1

Fig. 10. (a) Transmission electron micrograph (BFI) of the interlayer–YSZ interface in the steel/65Ag–20Cu–15Pd/YSZ joint. (b) Chemical compositions of the Cu-rich phase, the YSZ, Ti_3O_5 and SiO_2. (c, d) SADPs of (c) the Cu-rich phase (zone axis: [0 0 1]) and (d) the YSZ (zone axis: [0 1 1]). (e, f) Digital diffractograms obtained from high-resolution images of (e) amorphous SiO_2 and (f) Ti_3O_5 having a zone axis of [0 1 0].

between the interlayer and the YSZ. Another reaction product was Ti_3O_5, identified in the digital diffractogram of Fig. 9(f).

The EDS data in Fig. 9(b) revealed that 13 at.% of Al arose from an impurity of alumina in the YSZ, and that it diffused into Ti_3O_5. We believe that the source of Ti arose from the minor alloying constituents (e.g., Ti, P, Si, Ni) found in steel, because no Ti exists in the commercial Ag–Cu–Pd braze 58Ag–32Cu–10Pd. Owing to its higher affinity for oxygen, Ti atoms will diffuse across the interlayer and react with the YSZ to form Ti_3O_5 at the interface. From JCPDS (#82-1138), Ti_3O_5 is monoclinic with lattice parameters *a*, *b*, *c*, and β of 9.8 Å, 3.8 Å, 9.5 Å, and 93°, respectively; in 58Ag–32Cu–10Pd, however, these lattice parameters for Ti_3O_5 were 9.3 Å, 3.3 Å, 8.8 Å, and 97°, respectively. Residual stresses from the CTE mismatch between the YSZ and the interlayer would cause the

Ti_3O_5 crystal structure to slightly deform, leading to differences in the lattice parameters. The Gibbs free energies (ΔG) for Ti oxide formation have been proposed for the reactions of Ti with ZrO_2 [4,8]. Singh et al. indicated that the values of ΔG for oxide formation in the brazing temperature range 1193–1253 K for the various oxides of Ti (in kJ) were as follows: TiO_2 (−706.9 to −724.7), TiO (−417.5 to −428.5), Ti_4O_7 (−2590.7 to −2662.9), and Ti_3O_5 (−1878.9 to −1929.7). These negative values reveal that formation of titanium oxides is probable. In our present system, however, we observed evidence for the presence of Ti_3O_5, but not other Ti oxides. Although compounds such as Pd_3Zr, Pd_2Zr, PdZr, $PdZr_2$, Pd_3Y, Pd_2Y, Pd_3Y_2, and PdY can also form at relatively low (1073–1473 K) temperatures in Pd–Zr and Pd–Y systems, we found no evidence for any of these phases.

Fig. 10(a) displays a BFI of the interlayer–YSZ interface in a steel/65Ag–20Cu–15Pd/YSZ joint; dislocation substructures appeared in the Cu-rich phase and Ti_3O_5 and SiO_2 in the interlayer–YSZ interface were observed. The EDS data in Fig. 10(b) reveals that the Ti_3O_5 contained 11 at.% Al and the Cu-rich phase dissolved 16.4 at.% Zr, but the content of Pd was very low (0.2 at.%). Thus, the Cu-rich phase was FCC Cu and not Cu_3Pd. Fig. 10(c) and (d) present the SADPs of the Cu-rich phase with a zone axis of [0 0 1] and of the *t*-ZrO_2 with a zone axis of [0 1 1], respectively. A digital diffractogram obtained from a high-resolution image of SiO_2 [Fig. 10(e)] reveals that the crystal structure was amorphous. Fig. 10(f) provides a digital diffractogram obtained from a high-resolution image of the Ti_3O_5 with a [0 1 0] zone axis; from it, the lattice parameters were calculated as a, b, c, and β of 9.1 Å, 3.1 Å, 8.5 Å, and 93°, respectively.

4. Conclusions

Two commercial Ag-based interlayers containing Pd as an alloying element (58Ag–32Cu–10Pd and 65Ag–20Cu–15Pd) were used to join YSZ to a corrosion-resistant ferritic stainless steel. The SEM and TEM coupled with EDS to characterize the microstructures of the interlayer matrix and the interlayer–steel and interlayer–YSZ interfaces. In the interlayer matrix, the Cu-rich phase near the YSZ was FCC Cu; it dissolved a significant amount of Zr from ZrO_2 and minor amounts of Fe and Cr from the steel. The Cu-rich phase in the interlayer matrix near the steel was the ordered phase Cu_3Pd with APBs and an $L1_2$ crystal structure. Silver particles precipitated within the Cu_3Pd phase in the 58Ag–32Cu–10Pd interlayer; in contrast, a Fe(Cr) needle-like phase appeared in the Cu_3Pd phase in the 65Ag–20Cu–15Pd interlayer. No reaction products at the interlayer–steel interface were found, but dislocations did appear in the Ag- and Cu-rich phases. At the interlayer–YSZ interface, two reaction products: SiO_2 and Ti_3O_5 formed. Chemical interdiffusion among the YSZ, the steel, and the interlayer led to compositional changes and interfacial reconstruction induced by the reaction products, yielding metallurgically sound joints.

References

[1] S.C. Singhal, Solid oxide fuel cells for stationary, mobile, and military applications, Solid State Ionics 152–153 (2002) 405–410.

[2] S.P.S. Badwal, Stability of solid oxide fuel cell components, Solid State Ionics 143 (2001) 39–46.

[3] M.M. Schwartz, Joining of Composite–Matrix Materials, ASM International, Materials Park, OH, 1994, pp. 89–113.

[4] M. Singh, T.P. Shpargel, R. Asthana, Brazing of yttria-stabilized zirconia (YSZ) to stainless steel using Cu, Ag, and Ti-based brazes, J. Mater. Sci. 43 (2008) 23–32.

[5] W.B. Hanson, K.I. Ironside, J.A. Fernie, Active metal brazing of zirconia, Acta Mater. 48 (2000) 4673–4676.

[6] H.Q. Hao, Y.L. Wang, Z.H. Jin, X.T. Wang, Joining of zirconia to zirconia using Ag–Cu–Ti filler metal, J. Mater. Process. Technol. 52 (1995) 238–247.

[7] A.V. Durov, B.D. Kostjuk, A.V. Shevchenko, Y.V. Naidich, Joining of zirconia to metal with Cu–Ga–Ti and Cu–Sn–Pb–Ti fillers, Mater. Sci. Eng. A 290 (2000) 186–189.

[8] M. Singh, T.P. Shpargel, R. Asthana, Brazing of stainless steel to yttria-stabilized zirconia using gold-based brazes for solid oxide fuel cell applications, Int. J. Appl. Ceram. Technol. 4 (2) (2007) 119–133.

[9] M. Singh, T.P. Shpargel, R. Asthana, Braze oxidation behavior and joint microstructure in YSZ/steel joints, Mater. Sci. Eng. A 485 (2008) 695–702.

[10] J.T. Darsell, K.S. Weil, High-temperature strength of YSZ joints brazed with palladium–silver–copper oxide filler metals, Int. J. Hydrogen Energy 36 (7) (2011) 4519–4524.

[11] A.V. Durov, Y.V. Naidich, B.D. Kostyuk, Investigation of interaction of metal melts with zirconia, J. Mater. Sci. 40 (2005) 2173–2178.

[12] G. Cliff, G.W. Lorimer, The quantitative analysis of thin specimens, J. Microsc. 130 (3) (1975) 203–207.

[13] J.B. Liu, Y.W. Zeng, L. Meng, Interface structure and energy in Cu–71.8 wt.% Ag, J. Alloys Compd. 464 (2008) 168–173.

[14] D. Broddin, G. Van Tendeloo, J. Van Landuyt, S. Amelinckx, R. Porter, M. Guymont, A. Loiseau, Long-period superstructures in $Cu_{3\pm x}Pd$, Phil. Mag. A 54 (1986) 395–419.

[15] S. Takeda, J. Kulik, D. de Fontaine, Spinodal ordering beyond the Lifshitz point in Cu_3Pd observed by high voltage electron microscopy, Acta Metal. 35 (1987) 2243–2254.

[16] G. Ceder, D. de Fontaine, H. Dreysse, D.M. Nicholson, G.M. Stocks, B.L. Gyorffy, AB initio study of the Cu–Pd one-dimensional long period superstructure phase diagram, Acta Metal. Mater. 38 (1990) 2299–2308.

[17] Z. Guo, C.S. Lee, J.W. Morris Jr, On coherent transformations in steel, Acta Mater. 52 (2004) 5511–5518.

[18] L. Sandoval, H.M. Urbassek, P. Entel, The Bain versus Nishiyama–Wassermann path in the martensitic transformation of Fe, New J. Phys. 11 (2009) 103027.

[19] J.L. Murray, Calculations of stable and metastable equilibrium diagrams of the Ag–Cu and Cd–Zn systems, Metall. Trans. A 15 (1984) 261–268.

[20] K.L. Lin, C.C. Lin, Reaction between titanium and zirconia powders during sintering at 1500 °C, J. Am. Ceram. Soc. 90 (7) (2007) 2220–2225.

[21] S.P.S. Badwal, Grain boundary resistivity in zirconia-based materials: effect of sintering temperatures and impurities, Solid State Ionics 76 (1995) 67–80.